



Article

Suppressing the Photocatalytic Activity of TiO₂ Nanoparticles by Extremely Thin Al₂O₃ Films Grown by Gas-Phase Deposition at Ambient Conditions

Jing Guo ^{1,2,4}, Hao Van Bui ^{1,5,*} , David Valdesueiro ^{1,3}, Shaojun Yuan ², Bin Liang ² and J. Ruud van Ommen ¹

¹ Product & Process Engineering, Department of Chemical Engineering, Faculty of Applied Sciences, Delft University of Technology, 2629 HZ Delft, The Netherlands; guojing0519@hotmail.com (J.G.); d.valdesueiro@delft-imp.nl (D.V.); J.R.vanOmmen@tudelft.nl (J.R.v.O.)

² Multi-Phase Mass Transfer & Reaction Engineering Lab, College of Chemical Engineering, Sichuan University, Chengdu 610065, China; ysj@scu.edu.cn (S.Y.); liangbin@scu.edu.cn (B.L.)

³ Delft IMP B.V., Molengraaffsingel 10, 2629 JD Delft, The Netherlands

⁴ Shanxi Province Key Laboratory of Higeer-Oriented Chemical Engineering, North University of China, Taiyuan 030051, China

⁵ Department of Physics, Quy Nhon University, 170 An Duong Vuong Street, Quy Nhon City 590000, Vietnam

* Correspondence: V.H.Bui@tudelft.nl

Received: 23 November 2017; Accepted: 19 January 2018; Published: 24 January 2018

Abstract: This work investigated the suppression of photocatalytic activity of titanium dioxide (TiO₂) pigment powders by extremely thin aluminum oxide (Al₂O₃) films deposited via an atomic-layer-deposition-type process using trimethylaluminum (TMA) and H₂O as precursors. The deposition was performed on multiple grams of TiO₂ powder at room temperature and atmospheric pressure in a fluidized bed reactor, resulting in the growth of uniform and conformal Al₂O₃ films with thickness control at sub-nanometer level. The as-deposited Al₂O₃ films exhibited excellent photocatalytic suppression ability. Accordingly, an Al₂O₃ layer with a thickness of 1 nm could efficiently suppress the photocatalytic activities of rutile, anatase, and P25 TiO₂ nanoparticles without affecting their bulk optical properties. In addition, the influence of high-temperature annealing on the properties of the Al₂O₃ layers was investigated, revealing the possibility of achieving porous Al₂O₃ layers. Our approach demonstrated a fast, efficient, and simple route to coating Al₂O₃ films on TiO₂ pigment powders at the multigram scale, and showed great potential for large-scale production development.

Keywords: ultrathin Al₂O₃ films; atomic layer deposition; fluidized bed reactor; photocatalytic suppression; TiO₂ pigments

1. Introduction

The brilliant white color and high photostability of nanoparticulate titanium dioxide (TiO₂) make it an excellent white pigment in the paint, plastic, and paper industries [1]. In particular, TiO₂ has been widely used as a white pigment in oil paint since the 20th century, replacing lead white—the most important white pigment in history [2]. However, the high photocatalytic activity of TiO₂ under UV light irradiation causes the inevitable degradation of surrounding materials, which consequently changes the appearance and severely decreases the lifetime of the paintings. Depending on the surrounding materials, the photocatalytic degradation can occur via different regimes [3]. For instance, photocatalytic reactions can either promote polymerization of the organic binder, creating cross-linking that leads to embrittlement [4], or decompose the binder into volatile organic components, resulting

in surface roughening and chalking [5]. In addition, photocatalytic reactions can induce degradation of other organic colored pigments, which consequently leads to discoloration [6]. Photocatalytic degradation has also been observed for plastic art objects and photographic papers using TiO₂ as a white pigment [7]. Therefore, to avoid the photodegradation caused by the high catalytic activity of TiO₂, in these applications TiO₂ particles are commonly coated with a thin layer of a ceramic oxide, such as Al₂O₃ and SiO₂, with a thickness of a few nanometers [8–16]. On the one hand, owing to their good insulating properties, ultrathin layers of these oxides can provide efficient photocatalytic suppression by preventing the transport of electrons and holes generated by UV-light absorption to the surface. On the other hand, the large bandgap of the ceramic oxide materials ensures the optical transparency of the coating layers, and conserves the brilliant white color of TiO₂.

Ceramic oxide coating on TiO₂ pigments to mitigate their photocatalytic activity began in the early 1940s, using a precipitation technique [17]. Since then, a number of methods have been developed for the deposition of ultrathin coating layers. Wet chemistry methods, such as sol-gel and precipitation, have been most popular due to their simplicity, inexpensiveness, and versatility in depositing thin films of various materials. For example, thin films of single SiO₂ layer or binary Al₂O₃/SiO₂ layers can be obtained by precipitation [11], whereas sol-gel enables the deposition of various ceramic and transition metal oxides such as SiO₂, Al₂O₃, ZrO₂, NiO, and CoO with tunable morphology and properties [9,10,18,19]. However, wet chemistry methods have several shortcomings in controlling the coating thickness and conformity due to their high sensitivity to experimental parameters, such as precursor concentration, type and pH of the solvents, deposition time, and temperature. In addition, wet chemistry methods are time-consuming and commonly require post-treatment processes, for instance, high-temperature treatment, washing, drying, and separation to eliminate impurities arising from the residual solvent and reaction byproducts [9,10,14]. Moreover, when it comes to large-scale production, these techniques usually encounter environmental issues due to the use of a large amount of solvents and chemical solutions. Therefore, there has been a constant search for a simple, fast, environmentally friendly, and controllable deposition method that can overcome the drawbacks associated with wet chemistry methods, while being feasible for large-scale production.

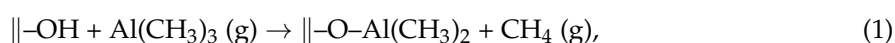
Atomic layer deposition (ALD) is a gas-phase deposition technique that is carried out using alternating exposures of the substrate to chemical reactants, each having self-limiting surface reactions that enable the control of film thickness at the atomic level [20–22]. ALD has been developed for a few decades [23,24], and utilized in the deposition of a wealth of materials on virtually every substrate for applications in various fields such as microelectronics, catalysis, and energy conversion and storage [21,25,26]. Particularly for coating on nanoparticles, ALD has emerged as an excellent method for the deposition of ultrathin conformal films of SiO₂ and Al₂O₃ [14,15,24,27–36]. In particular, recent developments in ALD reactor types, such as rotary and fluidized bed reactors (FBR), have enabled ALD of thin films on large quantities of micro- and nanoparticles [37–39]. Particularly, ALD of SiO₂ and Al₂O₃ on TiO₂ nanoparticles to mitigate their photocatalytic activities for pigment applications has been investigated by Weimer's research group [14,15,40]. Using tris-dimethylaminosilane (TMAS) and H₂O₂ as precursors, King et al. demonstrated that ultrathin conformal SiO₂ films could be deposited onto anatase/rutile TiO₂ powders with a growth-per-cycle (GPC) of approximately 0.04 nm at 500 °C [14]. Such an ALD-grown SiO₂ film with a thickness of 2 nm could suppress 98% of the photocatalytic activity of anatase TiO₂. However, the low GPC is not favorable for large-scale production development. A process based on siloxane polymerization using alternating exposures of tris(tert-pentoxysilanol) (TPS) and trimethylaluminum (TMA) enabled rapid SiO₂ ALD with a significantly high GPC of 1.8 nm at 170 °C [15]. Accordingly, a SiO₂ layer obtained for five cycles (i.e., ~9 nm) could entirely suppress the catalytic activity of TiO₂ pigments. Compared to the conventional SiO₂ ALD process [14], although a thicker film is needed to suppress the photocatalytic activity of TiO₂, which could be due to the lower mass density, the significantly lower deposition temperature and the remarkably higher GPC provide a fast and efficient deposition method that is suitable for upscaling. Meanwhile,

the mitigation of photocatalytic activity of TiO₂ by thin Al₂O₃ films deposited by ALD was also investigated. Hakim et al. demonstrated that an Al₂O₃ layer obtained for 50 ALD cycles at 170 °C (GPC of 0.2 nm) could suppress the high photocatalytic activity of P25 TiO₂ [40]. It is worth noting that, for pigment application, the thickness of the coating layer is of crucial importance: the layer must be thick enough to efficiently suppress the photocatalytic activity of TiO₂, but thin enough to conserve the gloss and brightness of TiO₂. This requires an optimal thickness, which is normally in the range of a few nanometers [17]. Therefore, reducing the coating thickness while ensuring its photocatalytic suppression ability is highly desirable.

This work reports on the suppression of photocatalytic activity of various types of TiO₂ powders (i.e., anatase, rutile, and P25 TiO₂) by Al₂O₃ films deposited via an ALD-like process using TMA and H₂O as precursors, which was carried out at room temperature and atmospheric pressure in a home-built fluidized bed reactor. This gas-phase deposition process enabled the control of coating thickness at the sub-nanometer level, allowing us to investigate the dependence of photocatalytic suppression ability of Al₂O₃ on the film thickness. The surface morphology and film thickness, composition, and crystallinity of the coating layers were characterized by transmission electron microscopy (TEM), X-ray photoelectron spectroscopy (XPS) and thermogravimetric analysis (TGA), and X-ray diffraction spectroscopy (XRD), respectively. The results showed that highly conformal Al₂O₃ films with a thickness as thin as 1 nm were obtained, which efficiently suppressed the photocatalytic activity of TiO₂ powders without affecting their bulk optical properties. Furthermore, the influence of high-temperature annealing on the properties of the Al₂O₃ layers was investigated, revealing the possibility to achieve porous Al₂O₃ layers, which could be useful for other applications.

2. Reaction Mechanism of Al₂O₃ ALD Using TMA and H₂O: A Brief Overview

The high reactivity of TMA facilitates the deposition of Al₂O₃ in a broad range of temperature on various types of substrates and materials with any geometries, including flat surfaces [21], high-aspect-ratio structures [41–43], porous media [44–47], nanoparticles [29,32,34,40], fibers [48], carbon nanotubes [49,50], graphene [51–53], polymers [54], and biomaterials [55]. The reaction mechanism in ALD of Al₂O₃ using TMA and H₂O has been intensively investigated in the past decades, both theoretically and experimentally [21,56–67]. Accordingly, the surface chemical reactions that lead to the deposition of Al₂O₃ in the ideal case can be divided into two half-reactions. During the exposure to TMA, the first half-reaction takes place and proceeds as:



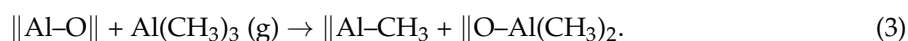
where the ||-OH represents the functional groups (i.e., hydroxyl groups), which are formed during the exposure of the substrate to air, or surface pretreatment. After all of the -OH groups have reacted with TMA, the reactions achieve saturation, forming a -CH₃ terminated surface, which is ready for the second half-reactions to take place during the exposure to H₂O, described as:



These reactions convert the -CH₃ into CH₄ and create a new surface terminated by -OH groups, which serves two purposes: blocking further reactions with H₂O, which causes saturation, and providing an active surface for the chemical reactions in the next cycle. A typical GPC in the range of 0.1–0.3 nm is obtained for TMA/H₂O ALD depending on experimental conditions such as temperature range, pressure range, and reactor type. The sequential exposures are repeated to deposit Al₂O₃ films, which translates into ability to control the film thickness at atomic level.

Nevertheless, the TMA/H₂O ALD chemistry is rather complex, which involves—apart from the ligand-exchange reactions described above—dissociation reactions that can take place in both the

half-reactions [21,68]. In the first half-reaction, TMA can react with unsaturated Al–O pairs of Al₂O₃ layers, creating a –CH₃ terminated surface described as [68]:



In the second half-reaction, dissociation reactions can occur between H₂O and the oxygen on Al₂O₃ surface, forming –OH surface functional groups, described as [21]:



The reversed reaction of the dissociation, the dehydroxylation, can also take place that consequently reduces the concentration of the OH groups, especially at high temperatures [21]:



Although the dissociation reactions are not often mentioned in the literature when discussing the surface chemistry in TMA/H₂O ALD, these reactions are believed to contribute considerably to growth. Especially, the dissociative chemisorption of TMA in the first half-cycle is the key mechanism that is used to interpret the nucleation on hydroxyl-free surfaces [59,60,69–72], even at room temperature [70]. In addition, at high deposition temperatures, the desorption of –OH groups and decomposition of TMA can occur simultaneously, which will strongly affect the growth rate of Al₂O₃ ALD [57,73]. Nevertheless, the ligand-exchange reactions are considered the dominant reactions during the deposition and have been most studied.

The GPC in ALD regime is generally temperature-independent, which is commonly known as “ALD window” [22]. However, ALD of Al₂O₃ using TMA/H₂O is found to be temperature-dependent [57,61,63,65]. Rahtu et al. [57] demonstrated a slight increase of GPC with increasing temperature from 150 to 250 °C, followed by a drop of GPC with further increase of temperature. The lower GPC at low temperature was attributed to the slow kinetics of the chemical reactions between the precursors, whereas the desorption of hydroxyl groups at high temperatures led to the drop of GPC. Most recently, the decrease of GPC at low deposition temperatures has been thoroughly investigated by Vandalon and Kessels [65]. Using in-situ vibrational sum-frequency generation technique, the authors investigated the reaction mechanism between TMA and H₂O in a broad temperature range (i.e., 100–300 °C), which revealed that the low GPC is caused by the incomplete removal of –CH₃ groups by H₂O at low temperature. The unreacted –CH₃ groups decline the chemisorption of TMA in the subsequent cycles, which consequently decreases the growth rate. The study also demonstrate that the persistent –CH₃ groups are not accumulated with increasing the number of cycles, which explains the low carbon impurity in Al₂O₃ layers grown by ALD at low temperatures [65]. Nevertheless, the experimental data obtained by Ylivaara et al. have demonstrated that the low-temperature deposition of Al₂O₃ using TMA and H₂O is inherently associated with a considerable amount of impurities, especially hydrogen and carbon, which increase with decreasing deposition temperature [74]. The hydrogen impurity arises from the unreacted hydroxyl groups, which has recently been verified by Guerra-Nunez et al. [66]. The degree of the GPC decrease at low temperatures is not well determined, and strongly depends on experimental conditions. For instance, contrary to the considerable drop of GPC at low temperatures observed by Vandalon and Kessels (i.e., the growth rate drops by approximately 50% when reducing the temperature from 250 to 100 °C), Groner et al. previously showed a slight decrease of GPC with decreasing temperature, even to near room temperature (i.e., 33 °C) [61]. The discrepancy between the studies can be attributed to the different ALD conditions, especially the process pressure range and reactor types.

3. Results and Discussion

3.1. Properties of the Al₂O₃ Coating Layers

3.1.1. Morphology of Al₂O₃-Coated TiO₂

We will first focus on the coating and performance of anatase TiO₂ powders. The morphology of the Al₂O₃ films on anatase TiO₂ for different exposure cycles is shown in Figure 1, demonstrating the deposition of uniform Al₂O₃ films, even at a film thickness of about 1 nm (Figure 1a). The coating thickness increases linearly with the number of cycles, with a GPC of approximately 0.3 nm (Figure 1d). The obtained GPC is higher than the GPC reported for ALD of Al₂O₃ on flat substrates, which is typically in the range of 0.1–0.2 nm [61,65]. However, this GPC value is lower than the GPC obtained for the Al₂O₃ ALD on particles (i.e., 0.5 nm) reported by Liang et al. [75]. Nevertheless, previous work from our group demonstrated that the growth of Al₂O₃ at room temperature and atmospheric pressure in FBR follows the chemical vapor deposition (CVD) mode, in which the GPC increases with increasing dosing time (i.e., without a self-saturating regime) [34]. With a GPC of 0.3 nm obtained for the examined conditions, a controlled deposition at sub-nanometer level of highly conformal Al₂O₃ films is totally achievable. In fact, this higher GPC is beneficial for the fast and scalable production that is required for practical applications.

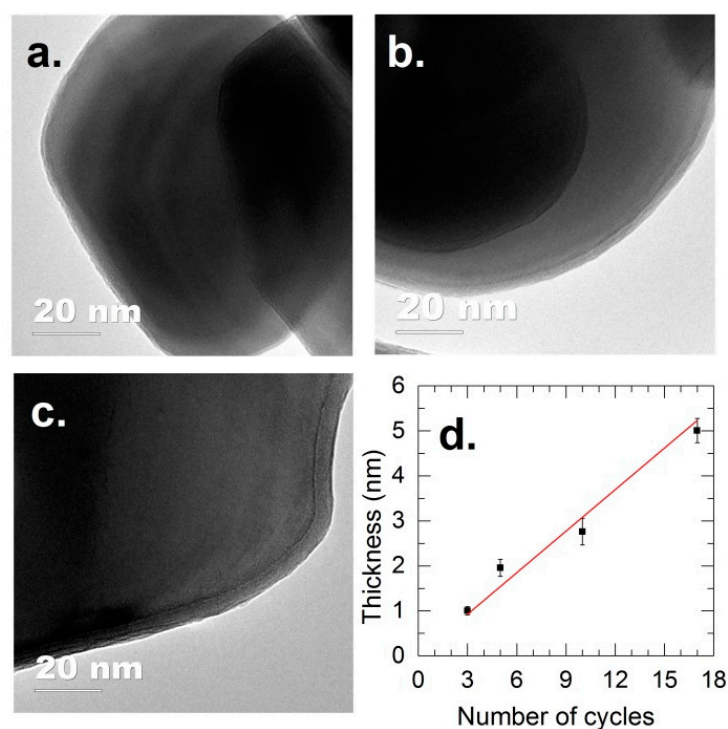


Figure 1. TEM images of Al₂O₃ films deposited on anatase TiO₂ nanoparticles for (a) three cycles, (b) 10 cycles and (c) 17 cycles, and (d) the coating thickness as a function of the number of cycles.

3.1.2. Structural and Optical Properties of Room-Temperature-Grown Al₂O₃

The chemical states of the initial TiO₂ surface are characterized by XPS and shown in Figure 2. The fingerprints of TiO₂ are featured by the peaks at binding energies (BE) of 529.4 eV (O 1s, Figure 2a), BE = 463.9 eV and BE = 458.2 eV (Ti 2p, Figure 2c). The deconvolution of O 1s spectrum revealed the presence of a considerable amount of –OH groups (BE = 530.8 eV) and physisorbed H₂O (BE = 532.3 eV) [76,77]. The physisorbed H₂O can be removed by applying a heat treatment in air at 170 °C for 1 h, as indicated by Figure 2b. We note that no distinguishable difference was observed for

the growth of the Al_2O_3 on the TiO_2 without and with heat treatment. However, the existence of $-\text{OH}$ groups on the surface is important to the inception of TMA chemisorption. The C 1s spectrum exhibits different states of C contamination (Figure 2d), including $\text{C}=\text{O}$ (BE = 288.6 eV), $\text{O}-\text{C}$ (BE = 286.2 eV) and $\text{C}=\text{C}$ (BE = 284.7 eV) [76,78]. These carbon compounds could arise from adsorbed species on the surface of the powders and/or the carbon tape used to immobilize the TiO_2 particles.

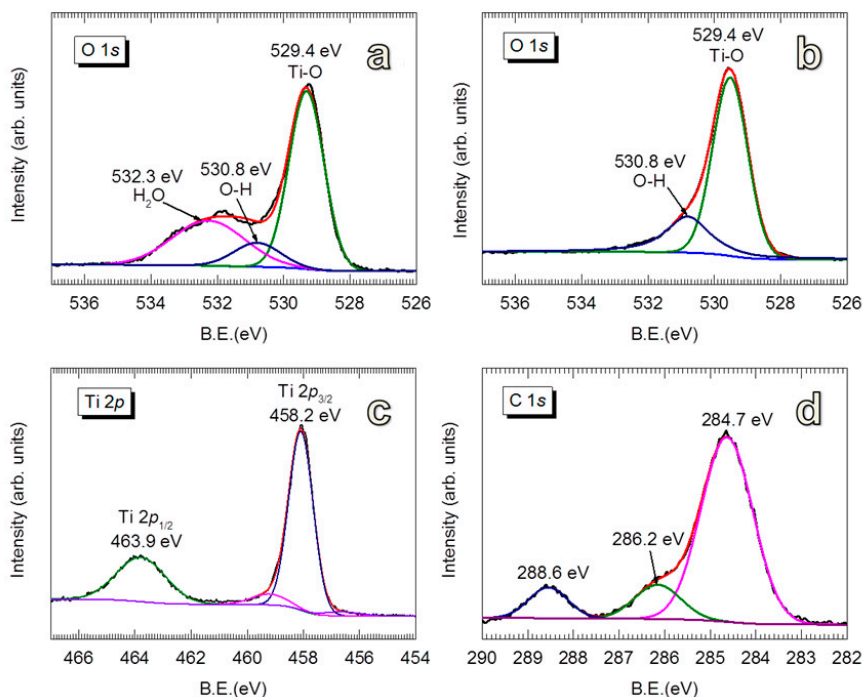


Figure 2. XPS spectra of uncoated anatase TiO_2 powders: O 1s (a) without and (b) with preheating (at $170\text{ }^\circ\text{C}$ in air), (c) Ti 2p and (d) C 1s.

For the Al_2O_3 -coated TiO_2 , the BE = 531.6 eV (for O 1s, Figure 3a,b) and BE = 74.3 eV (for Al 2p, Figure 3c,d) represent the Al–O bonds in Al_2O_3 compounds [78–80]. No noticeable change was observed for the BE of Al 2p with increasing coating thickness. However, the peaks of TiO_2 (i.e., BE = 529.4 eV for O 1s, BE = 463.9 eV for Ti $2p_{1/2}$, and BE = 458.2 eV for Ti $2p_{3/2}$) are gradually attenuated with increasing Al_2O_3 thickness. For the TiO_2 coated with 5 nm Al_2O_3 , the TiO_2 peaks are almost vanished, which suggests that the photoelectrons of TiO_2 excited by the X-rays are effectively shielded by the Al_2O_3 film. The disappearance of TiO_2 features in XPS spectra is evidence of uniform Al_2O_3 coating on a large scale, in addition to the evidence provided by the TEM micrographs shown in Figure 1. Furthermore, the gradual attenuation of C 1s at BE = 288.6 eV ($\text{C}=\text{O}$) and BE = 286.2 eV ($\text{O}-\text{C}$) relatively compared to the peak at BE = 284.7 eV ($\text{C}=\text{C}$) with increasing Al_2O_3 thickness can be explained that these carbon-containing species are on the surface of TiO_2 . This, however, does not rule out the possibility that the carbon content is accumulating in the growing film, which cannot be avoided due to the deposition at room temperature.

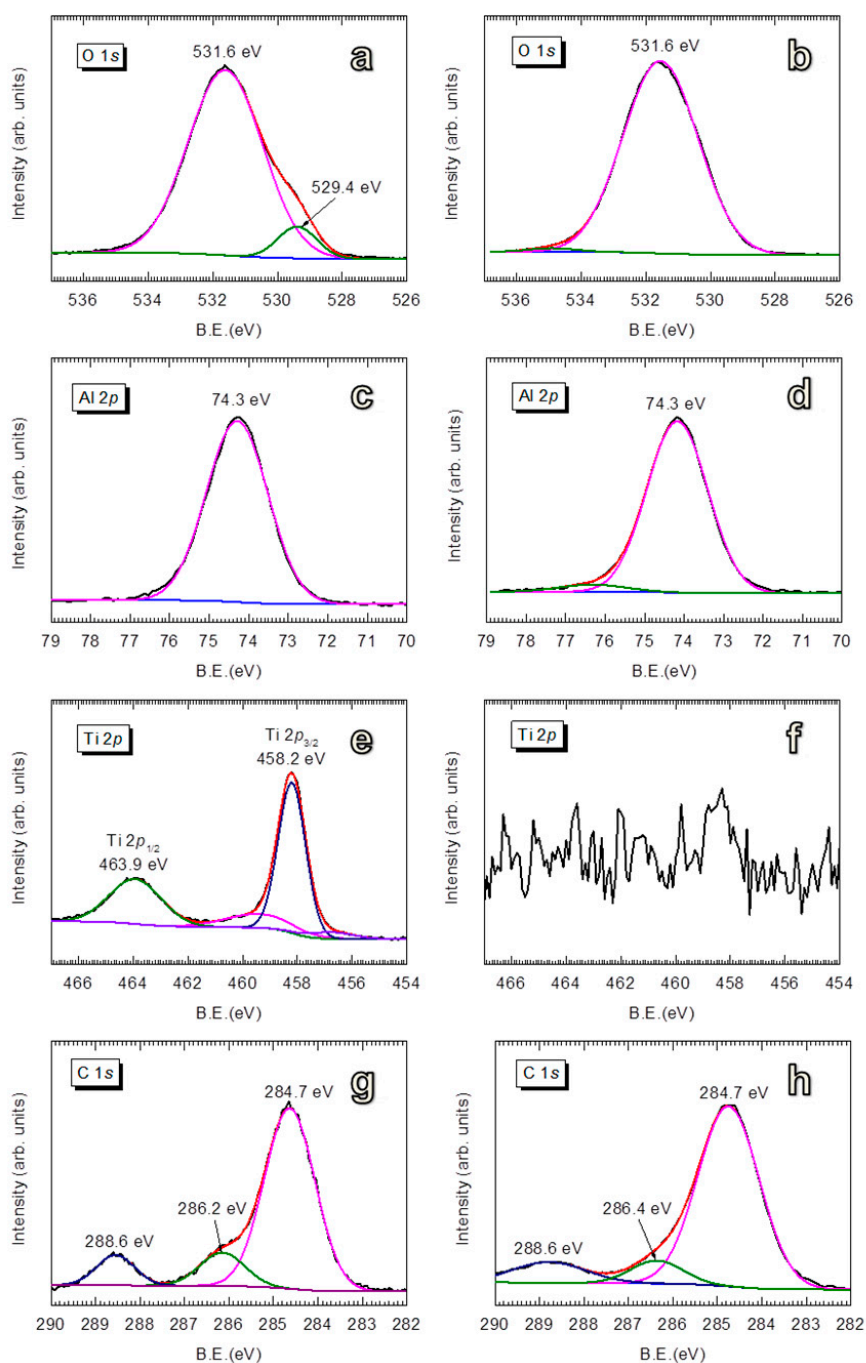


Figure 3. XPS spectra of anatase TiO₂ coated with 3 nm thick (a,c,e,g—on the left side) and 5 nm thick (b,d,f,h—on the right side) Al₂O₃ films.

As a photocatalytic suppression layer for pigment applications, the transparency of the coating layer, which is crucially important to maintain the bulk optical properties of TiO₂ such as the white color and high brightness, is highly desirable. The optical absorption spectra shown in Figure 4 indicate that the absorption of TiO₂ remained unaffected upon the coating with Al₂O₃ with different film thicknesses. From the absorption spectra, an optical bandgap of 3.2 eV was determined, which corresponds to that of anatase TiO₂ [81]. The characterization using X-ray diffraction showed the amorphous state of the Al₂O₃ layers, even after annealing at 500 °C for 12 h (Figure S1).

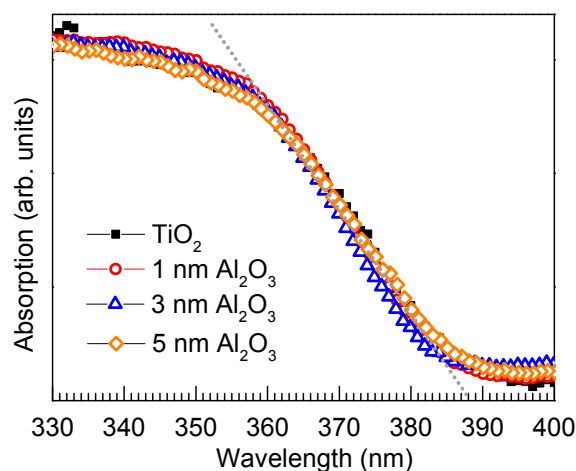


Figure 4. Absorption spectra of pristine anatase TiO_2 powder and the TiO_2 coated with Al_2O_3 films with different thicknesses: 1 nm, 3 nm, and 5 nm.

3.1.3. Thermogravimetric Analysis

Figure 5a shows TGA plots of the TiO_2 powders coated with Al_2O_3 films with different thicknesses. The first stage (i.e., $T \leq 120$ °C) describes the desorption of water when the powders are heated from 25 °C, showing an increasing amount of water with Al_2O_3 thickness. The second stage demonstrates the desorption of hydroxyl groups, which increases remarkably with increasing the coating thickness. Following the calculation method proposed by Pratsinis et al., from the TGA plots shown in Figure 5a, the density of $-\text{OH}$ groups was estimated by following the common assumption that all the $-\text{OH}$ groups are on the surface [82,83]. For uncoated TiO_2 , a density of 4 $-\text{OH}/\text{nm}^2$ was obtained, which is close to the value reported for anatase TiO_2 [83]. On Al_2O_3 -coated TiO_2 , the density of $-\text{OH}$ groups increased linearly with Al_2O_3 thickness (Figure 5b): a density of 9.6 $-\text{OH}/\text{nm}^2$ was obtained for the 1 nm thick Al_2O_3 coated powder, and increased to 95.3 $-\text{OH}/\text{nm}^2$ for the TiO_2 coated with 5 nm Al_2O_3 . As this number is not reasonable for the assumption that all the $-\text{OH}$ groups are on the surface of the powder (i.e., it is theoretically and practically impossible to have 95 $-\text{OH}$ groups on 1 nm^2), the calculated values suggest that most of the $-\text{OH}$ groups are located inside the coating layer. This is caused by the incomplete consumption of $-\text{OH}$ groups, which leads to hydrogen impurity in the film [66]. The existence of $-\text{OH}$ strongly affects the density of Al_2O_3 [61]. Nevertheless, Groner et al. [61] demonstrated that the Al_2O_3 films grown at low temperatures exhibited excellent electrical properties despite containing high $-\text{OH}$ concentrations. As we will demonstrate later, despite having high densities of $-\text{OH}$ groups, ultrathin Al_2O_3 films deposited at room temperature can provide excellent photocatalytic suppression ability.

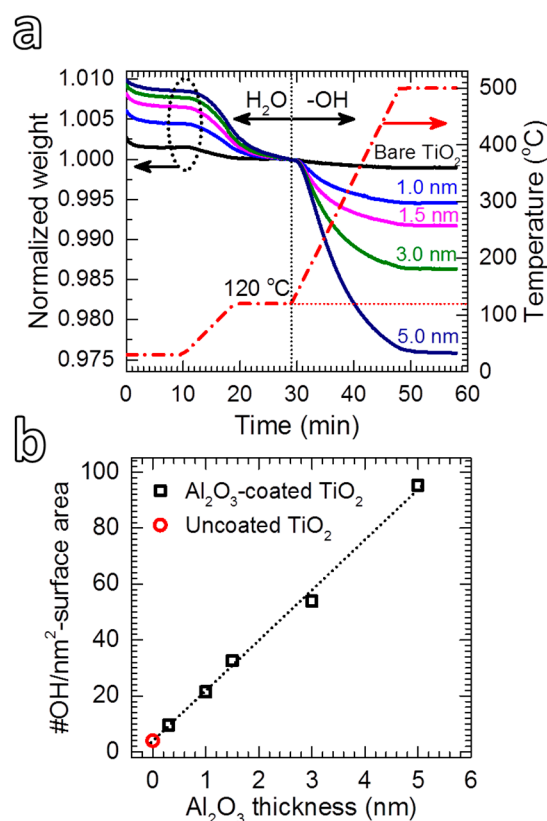


Figure 5. (a) TGA curves of uncoated and Al₂O₃-coated anatase TiO₂ powders and (b) the density of hydroxyl groups as a function of Al₂O₃ thickness.

3.2. Photocatalytic Activity of Al₂O₃-Coated TiO₂

3.2.1. Dependence of Photocatalytic Suppression Ability of Al₂O₃ on Film Thickness

The photocatalytic suppression ability of the room-temperature grown Al₂O₃ was investigated by the photodegradation of rhodamine B (RhB) solution under the irradiation of sunlight generated by a solar simulator. The ability to control the growth at sub-nanometer level allowed us to study the interdependence of the photocatalytic suppression ability and the thickness of Al₂O₃. Figure 6 shows the photocatalytic activity toward the photodegradation of RhB of TiO₂ powders coated with Al₂O₃ films with different thicknesses. For comparison, the self-degradation of RhB (i.e., without TiO₂) caused by the UV light and the photocatalytic activity of uncoated TiO₂ were also investigated. Prior to the UV irradiation, the solution was continuously stirred in the dark (i.e., light-off stage) for 30 min to obtain adsorption/desorption equilibrium of RhB and uniform suspensions, which were collected after certain time-intervals to determine the concentration of the residual RhB. The results showed that during the light-off stage, the concentration of RhB in the solution without TiO₂ powders (blank RhB) remained unchanged. However, a small drop of RhB concentration was observed for the solutions with TiO₂ powders (both uncoated and coated with Al₂O₃). This drop is due to the adsorption of a fraction of RhB molecules on the surface of the particles. Shortly after that (i.e., after 2 min) the concentration of RhB reached the steady state. In the light-on stage, a rapid decomposition of RhB in the solution containing uncoated TiO₂ was observed (the circles in Figure 6a), and after 25 min of irradiation, the RhB was completely decomposed, indicative of the high photocatalytic activity of the TiO₂.

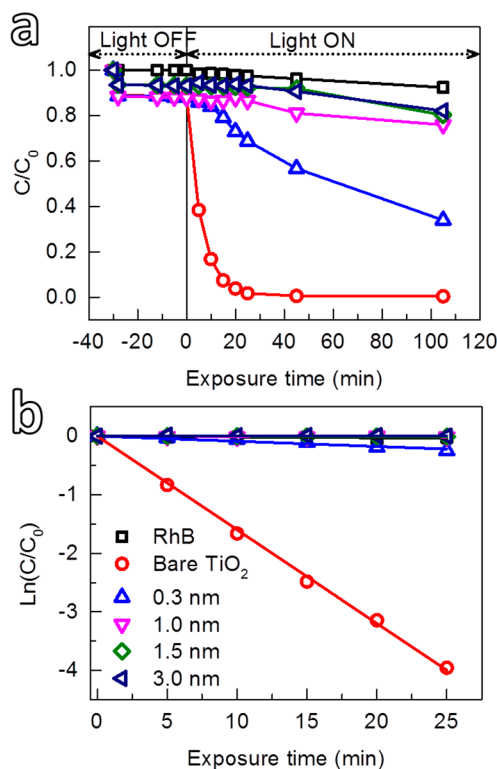


Figure 6. (a) Photodegradation of RhB solution using anatase TiO_2 coated with Al_2O_3 films with different thicknesses as a function of exposure time, and (b) the corresponding kinetic reaction plots.

For the Al_2O_3 -coated TiO_2 , the photocatalytic activity was reduced, which exhibited a strong dependence on the thickness of the Al_2O_3 layer. This thickness dependence can be quantitatively estimated by the kinetics of the photodegradation reaction, which can be described by first-order kinetics [84]:

$$\ln(C_0/C) = k_{app} \cdot t, \text{ or } C = C_0 \cdot \exp(-k_{app} \cdot t), \quad (6)$$

where C_0 and C are the initial concentration and the concentration at the time t , respectively, k_{app} is the apparent first-order kinetic constant that represents the reaction rate. The kinetic plots describing the degradation of RhB are shown in Figure 6b, from which the k_{app} value for each reaction was extracted and presented in Table 1. Accordingly, the photocatalytic activity of TiO_2 ($k_{app} \approx 160 \times 10^{-3} \text{ min}^{-1}$) was reduced approximately 18 times (to $k_{app} \approx 8.87 \times 10^{-3} \text{ min}^{-1}$) by coating an Al_2O_3 layer for 1 cycle of TMA and H_2O exposures (i.e., the calculated thickness of about 0.3 nm). Nevertheless, the Al_2O_3 at this thickness cannot entirely suppress the photocatalytic activity of TiO_2 . This could be due to (1) the insufficient thickness that can block the transport of photogenerated charges from the TiO_2 to the surface, and/or (2) the lack of continuity of the coating layer. With increasing film thickness, k_{app} value decreased rapidly, which dropped to far below $1 \times 10^{-3} \text{ min}^{-1}$ for Al_2O_3 films with a thickness of 1 nm or thicker (thickness $a \geq 1 \text{ nm}$). The results showed that an Al_2O_3 layer with a thickness of 1 nm efficiently suppressed entirely the catalytic activity of the TiO_2 . The degradation of RhB observed for the TiO_2 coated with Al_2O_3 films with thickness $a \geq 1 \text{ nm}$ is identical to that of the self-degradation of RhB solution without the powder (Figure 6b and Table 1). A comparison with other coating processes and materials that have been used to mitigate the photocatalytic activity of TiO_2 pigments is given in Table 2. It can be seen that gas-phase deposition methods such as ALD and CVD have been employed. However, the reported processes were carried out at much higher temperatures, i.e., above $150 \text{ }^\circ\text{C}$ for Al_2O_3 and $175 \text{ }^\circ\text{C}$ for SiO_2 . In addition, thicker layers are needed to efficiently suppress the photocatalytic activity of TiO_2 , which is also the case for the layer obtained by wet-chemistry methods. This indicates that our approach has significant advantages in providing

a fast and efficient coating method that can be carried out at room temperature, which increases the feasibility for further development to large-scale production.

Table 1. Apparent first-order rate constant, k_{app} , of anatase TiO₂ powders coated with Al₂O₃ with different film thicknesses.

Sample	$k_{app} \times 10^3/\text{min}^{-1}$		R^2 of Fitting	
	As-Deposited	Calcined	As-Deposited	Calcined
RhB	0.52 ± 0.03	0.52 ± 0.03	0.99	0.99
Uncoated TiO ₂	160 ± 1.60	100 ± 4.12	1.00	0.99
0.3 nm Al ₂ O ₃ coated TiO ₂	8.87 ± 0.71	19.3 ± 0.03	0.96	0.99
1.0 nm Al ₂ O ₃ coated TiO ₂	0.64 ± 0.21	7.07 ± 0.53	0.90	0.96
1.5 nm Al ₂ O ₃ coated TiO ₂	0.41 ± 0.02	4.77 ± 0.68	0.99	0.89
3.0 nm Al ₂ O ₃ coated TiO ₂	0.35 ± 0.03	3.27 ± 0.80	0.98	0.72

Table 2. Coating methods and materials for suppressing photocatalytic activity of TiO₂ pigments.

TiO ₂ Material	Average Diameter (nm)	Coating Method	Coating Material	Coating Thickness (nm)	Deposition Temperature (°C)	Photocat. Reaction	Ref.
P25	21	ALD	Al ₂ O ₃	6.0	177	Methylene blue	[40]
Anatase Rutile	160 280	ALD	SiO ₂ SiO ₂ /Al ₂ O ₃ SiO ₂ /Al ₂ O ₃ /SiO ₂ /Al ₂ O ₃	2.0 1.0/1.0 0.5/0.5/0.5/0.5	500 for SiO ₂ 177 for Al ₂ O ₃	IPA to acetone	[14]
P25	21	ALD	Al ₂ O ₃	3.8	150	RhB	[85]
Anatase P25	160 18	ALD	SiO ₂	6.0 9.0	175	Methylene blue	[15]
Anatase	160	MLD	Alucone	7–10	100–160	Methylene blue	[86]
Rutile	Not reported	CVD	SiO ₂	1–2	900–1000	Methylene blue	[13]
Rutile	300	Wet-chemistry	ZrO ₂ CeO ₂	5.0 1–2	40 60	RhB	[19]
Rutile	300	Wet-chemistry	CeO ₂	1–2	60	RhB	[87]
ST-21	20	Wet-chemistry	SiO ₂	4.0	40	Methylene blue	[8]
P25	21	Wet-chemistry	Porous SiO ₂	20.0	Room temperature	RhB	[10]
Anatase Rutile P25	270 300 21	ALD-like	Al ₂ O ₃	1.0	Room temperature	RhB	This work

3.2.2. Influence of High-Temperature Calcination on Photocatalytic Suppression Ability of Al₂O₃

As demonstrated by the thermal analysis shown in Figure 5, the room-temperature-grown Al₂O₃ films contain a high density of –OH groups, which can desorb at high temperatures. Therefore, a calcination at 500 °C for 12 h was applied to investigate the influence of the –OH desorption on the suppression ability of Al₂O₃. The results show that the calcination of Al₂O₃-coated TiO₂ resulted in an enhanced photocatalytic activity (Figure S2), in which k_{app} values increased nearly an order of magnitude (Table 1). This indicates that the –OH desorption reduced the suppression ability of the Al₂O₃ layer. We speculate that the desorption of –OH groups resulted in the formation of porous Al₂O₃ that allows photogenerated electrons to transport to the surface. In addition, the densification, which may introduce cracks during calcination, can also take place and increase the porosity of the Al₂O₃ [74]. This is supported by the XPS spectra of the calcined Al₂O₃/TiO₂ shown in Figure S3. Accordingly, the two XPS peaks of the Ti 2p core-levels that were attenuated after coating with a 5-nm Al₂O₃ film

were partially recovered after the calcination, which suggests that the photoelectrons generated by the X-rays could travel through the calcined Al_2O_3 layer. For uncoated TiO_2 , the results show that the $-\text{OH}$ desorption reduced the photocatalytic activity (Figure S2), indicated by the drop of k_{app} from 160×10^{-3} to $100 \times 10^{-3} \text{ min}^{-1}$ (Table 1). This can be explained by the fact that in TiO_2 photocatalysis, hydroxyl groups act as hole traps, which causes two important effects that enhance the photocatalytic activity: enhancement of charge separation and formation of hydroxyl radicals [76,88–90].

3.2.3. Photocatalytic Suppression Ability of Al_2O_3 on P25 and Rutile TiO_2

Analogously to the deposition on anatase TiO_2 , uniform Al_2O_3 films were also achieved on rutile and P25 TiO_2 powders (Figures S4 and S5), which enabled the study on photocatalytic suppression ability of the Al_2O_3 films on P25 and rutile TiO_2 nanoparticles. The results are demonstrated in Figure 7. The photocatalytic activity of rutile TiO_2 ($k_{\text{app}} \approx 4.85 \times 10^{-3} \text{ min}^{-1}$) is much lower than that of anatase TiO_2 ($k_{\text{app}} \approx 159.88 \times 10^{-3} \text{ min}^{-1}$) under identical conditions, which is also known from the literature [90,91]. After coating the rutile particles with 1 nm Al_2O_3 , the photocatalytic activity is strongly suppressed, which is confirmed by the low k_{app} value obtained ($0.28 \times 10^{-3} \text{ min}^{-1}$). In contrast, the photocatalytic activity of P25 TiO_2 ($k_{\text{app}} \approx 231 \times 10^{-3} \text{ min}^{-1}$) was found to be higher than that of anatase TiO_2 . Nevertheless, by coating with an Al_2O_3 layer with a thickness of approximately 1 nm, the photocatalytic activity of P25 was also strongly suppressed ($k_{\text{app}} \approx 2.01 \times 10^{-3} \text{ min}^{-1}$). These results have further demonstrated the high photocatalytic suppression ability of the ultrathin Al_2O_3 films deposited under mild conditions.

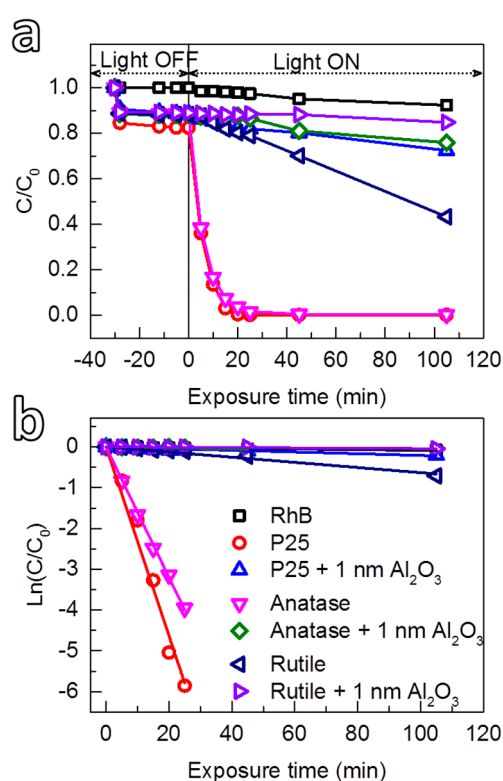


Figure 7. (a) Photodegradation as a function of exposure time of RhB solution by uncoated TiO_2 (P25, anatase and rutile) and the TiO_2 coated with 1 nm Al_2O_3 , and (b) the corresponding kinetic plots. All of the photocatalytic tests were carried out under identical experimental conditions. The self-degradation of RhB is added as the reference.

4. Experimental Section

The deposition was carried out in a home-built fluidized bed reactor operating at atmospheric pressure and room temperature, as described elsewhere [34]. Briefly, the system consisted of a glass column (26 mm in internal diameter and 500 mm in height) placed on top of a single motor Paja PTL 40/40–24 vertical vibration table to assist the fluidization of nanoparticles. Anatase (mean diameter $d \approx 270$ nm) and rutile (mean diameter $d \approx 300$ nm) TiO₂ pigment powders were provided by Taihai TiO₂ Pigment Co. (Panzhuhua, China); aerioxide P25 TiO₂ (mean diameter $d \approx 21$ nm) were purchased from Evonik Industries (Hanau, Germany). Semiconductor grade trimethylaluminum (TMA) was provided by Akzo Nobel HPMO (Amersfoort, The Netherlands) in a 600 mL WW-600 stainless steel bubbler. Both the TiO₂ powders and the TMA precursor were used as received. Pressurized nitrogen (99.999 vol %) was used as the carrier gas. For each experiment on anatase and rutile TiO₂, 7.0 g of powders was used. An optimized N₂ gas flow of 0.5 L min⁻¹ was introduced through the distributor plate placed at the bottom of the glass column to fluidize the powders. A coating cycle consisted of alternating exposures of the powders to TMA precursor (2 min) and deionized water vapor (2 min), separated by a purging step (5 min) using N₂. The coating on P25 followed the conditions described elsewhere [34]. The temperature inside the bed was monitored by a type-K thermocouple inserted in the column, which showed a small variation during the deposition (i.e., 27 ± 3 °C), possibly due to the heat release from the chemical reactions.

As-coated Al₂O₃/TiO₂ powders were suspended in ethanol and transferred to regular transmission electron microscopy (TEM) grids (3.05 mm in diameter). TEM images were taken at several locations on the grids using a JEOL JEM1400 transmission electron microscope (JEOL, Peabody, MA, USA) operating at a voltage of 120 kV and a current density of 50 pA cm⁻².

X-ray photoelectron (XPS) characterizations were carried out using a ThermoFisher K-Alpha system (ThermoFisher Scientific, Waltham, MA, USA) using Al K α radiation with photon energy of 1486.7 eV. A sufficient amount of powder was immobilized on carbon tape before loading into the XPS chamber. Survey scans were acquired using a 200 μ m spot size, 55 eV pass energy and 0.1 eV/step with charge neutralization. The peaks positions were calibrated according to the C 1s peak at 284.7 eV.

A Mettler Toledo TGA/SDTA 851e thermogravimetric analyzer (Mettler Toledo B.V., Tiel, The Netherlands) was used for studying the thermal behavior of the synthesized powders. An amount of 30 mg of powders was used for each TGA measurement. The TGA curves were recorded while (1) heating up the powders from 25 to $T_1 = 120$ °C with a ramping rate of 10 °C min⁻¹ in a N₂ flow of 100 mL min⁻¹; (2) maintaining at 120 °C for 10 min; (3) ramping up to 500 °C with a ramping rate of 20 °C min⁻¹; and (4) finally maintaining at this temperature for 10 min. Steps (1) and (3) are commonly used to determine the density of physisorbed water and chemisorbed hydroxyl groups on the surface, respectively [83].

The Al₂O₃/TiO₂ was transferred onto a Si wafer with 300 nm of SiO₂ thermal oxide, which was to eliminate the influence of the substrate (Si) signal in the X-ray diffractograms of the powders. The X-ray diffractograms were obtained by a PANalytical X'pert Pro diffractometer (PANalytical, Almelo, The Netherlands) with Cu K α radiation, secondary flat crystal monochromator and X'celerator RTMS Detector system. The angle of interest 2θ was measured from 10° to 90° with fine steps of 0.001°.

Optical absorption measurements were performed using a PerkinElmer-Lambda 900 spectrometer (PerkinElmer, Spokane, WA, USA) equipped with an integrated sphere device. The powder was suspended in ethanol, which was transferred onto a quartz substrate and dried in air. The spectra were acquired in the wavelength range of 600–200 nm, with fine steps of 1 nm.

The photocatalytic activity of the Al₂O₃-coated TiO₂ powders was evaluated by the photodegradation of RhB solution. For each test, 30 mg of the powders were added to 30 mL RhB solution (concentration of 8 mg L⁻¹) and continuously stirred in the dark for 30 min to obtain a uniform suspension. Thereafter, the suspension was exposed to UV radiation generated by a mercury lamp with a power of 45 W for different exposure times. The set-up allowed us to assess up to 10 samples simultaneously, which ensured that all samples were irradiated under the same conditions, such as

light intensity, exposure time, and temperature. The suspension was then centrifuged to separate the powders from the solution. Finally, the solution was analyzed by UV-visible spectrophotometry (HACH LANGE DR5000 UV-vis spectrometer, Hach-Lange GmbH, Düsseldorf, Germany) to determine the residual concentration of the RhB in solution, which was used to evaluate the catalytic activity suppression of the Al₂O₃ layers.

5. Conclusions

We have demonstrated the deposition and investigated the photocatalytic suppression ability of ultrathin Al₂O₃ films on different types of TiO₂ powders: anatase (mean diameter $d \approx 270$ nm), rutile (mean diameter $d \approx 300$ nm) and P25 (mean diameter $d \approx 21$ nm). The deposition was carried out using an ALD-like process, in which the TiO₂ powders were alternatively exposed to TMA and H₂O at room temperature and atmospheric pressure in a FBR. This enabled the deposition of ultrathin, conformal and uniform Al₂O₃ films with the thickness control at sub-nanometer level. The deposition at room temperature resulted in amorphous Al₂O₃ layers containing a high concentration of hydroxyl groups, which was caused by the incomplete reactions between the precursors at low temperature. Nevertheless, the films exhibited excellent photocatalytic suppression ability, which showed that an Al₂O₃ layer with a thickness of 1 nm could efficiently suppress the photocatalytic activities of the TiO₂ powders. In addition, the optical absorption of TiO₂ was not affected by the Al₂O₃ coating. Upon calcination at a high temperature, photocatalytic suppression ability of the Al₂O₃ was decreased, possibly due to the formation of porous Al₂O₃ layer, which created pathways for charge carriers to transport to the surface. Our approach of using a FBR operating at atmospheric pressure is a fast, efficient, simple method for depositing ultrathin conformal Al₂O₃ films that meet the requirements for coating pigments, which can be further developed for large-scale production.

Supplementary Materials: The following are available online at www.mdpi.com/2079-4991/8/2/61/s1, Figure S1: XRD patterns of uncoated TiO₂ and Al₂O₃-coated TiO₂, with or without annealing at 500 °C for 12 h. Figure S2: The comparison of photocatalytic activity of Al₂O₃/TiO₂ (anatase) powders before and after annealing at 500 °C for 12 h. Figure S3: XPS spectra of C 1s, Al 2p, O 1s and Ti 2p core-levels of anatase TiO₂ coated with 5 nm Al₂O₃ as-deposited and after annealing at 500 °C for 12 h in air. Figure S4: TEM micrographs of rutile TiO₂ coated with Al₂O₃ films deposited for 3 cycles, 5 cycles, 10 cycles and 17 cycles. Figure S5: High-resolution TEM micrographs of P25 TiO₂ nanoparticles coated with Al₂O₃ for 4 cycles, 7 cycles and 15 cycles.

Acknowledgments: We acknowledge our colleagues at Delft University of Technology, Damiano La Zara (PPE, ChemE) for XPS measurements, Thang Nguyen (FAME, Reactor Institute Delft) for XRD analyses, Bart van der Linden (Catalysis Engineering, ChemE) for TGA characterizations, and Varsha Pridhivi (PPE, ChemE) for optical absorption spectroscopy measurements. The authors would like to acknowledge the financial support from the China Scholarship Council, the key project of National Natural Science Foundation of China (No. 21236004), and the European Research Council under the European Union's Seventh Framework Program (FP/2007-2013)/ERC Grant, Agreement No. 279632.

Author Contributions: J.R.v.O., B.L. and S.Y. initiated the research; J.G., D.V. and H.V.B. designed and performed the experiments, and analyzed the data under the supervision of J.R.v.O. and B.L.; J.G. and H.V.B. wrote the paper with the feedback for editing from all authors.

Conflicts of Interest: The authors declare no conflict of interest.

References

1. Shi, H.; Magaye, R.; Castranova, V.; Zhao, J. Titanium dioxide nanoparticles: A review of current toxicological data. *Part. Fibre Toxicol.* **2013**, *10*, 15–47. [[CrossRef](#)] [[PubMed](#)]
2. Gettens, R.J.; Kühn, H.; Chase, W.T. Lead white. *Stud. Conserv.* **1967**, *12*, 125–139.
3. Van Driel, B.A.; Wezendonk, T.A.; van den Berg, K.J.; Kooyman, P.J.; Gascon, J.; Dik, J. Determination of early warning signs for photocatalytic degradation of titanium white oil paints by means of surface analysis. *Spectrochim. Acta Part A* **2017**, *172*, 100–108. [[CrossRef](#)] [[PubMed](#)]
4. Yousif, E.; Haddad, R. Photodegradation and photostabilization of polymers, especially polystyrene: Review. *SpringerPlus* **2013**, *2*, 398. [[CrossRef](#)] [[PubMed](#)]

5. Völz Hans, G.; Kaempf, G.; Fitzky, H.G.; Klaeren, A. The chemical nature of chalking in the presence of titanium dioxide pigments. In *Photodegradation and Photostabilization of Coatings*; Winslow, F.H., Ed.; ACS Symposium Series; ACS Publishing: Washington, DC, USA, 1981; Volume 151, pp. 163–182.
6. Samain, L.; Silversmit, G.; Sanyova, J.; Vekemans, B.; Salomon, H.; Gilbert, B.; Grandjean, F.; Long, G.J.; Hermann, R.P.; Vincze, L.; et al. Fading of modern prussian blue pigments in linseed oil medium. *J. Anal. At. Spectrom.* **2011**, *26*, 930–941. [[CrossRef](#)]
7. Van Driel, B.A.; Kooyman, P.J.; van den Berg, K.J.; Schmidt-Ott, A.; Dik, J. A quick assessment of the photocatalytic activity of TiO₂ pigments—From lab to conservation studio! *Microchem. J.* **2016**, *126*, 162–171. [[CrossRef](#)]
8. Lee, H.; Koo, S.; Yoo, J. TiO₂–SiO₂ nanoparticles for suppressing photocatalytic activities and improving hydrophilicity. *J. Ceram. Process. Res.* **2012**, *13*, S300–S303.
9. Park, O.K.; Kang, Y.S. Preparation and characterization of silica-coated TiO₂ nanoparticle. *Colloids Surf. A* **2005**, *257*, 261–265. [[CrossRef](#)]
10. Ren, Y.; Chen, M.; Zhang, Y.; Wu, L. Fabrication of rattle-type TiO₂/SiO₂ core/shell particles with both high photoactivity and UV-shielding property. *Langmuir* **2010**, *26*, 11391–11396. [[CrossRef](#)] [[PubMed](#)]
11. Liu, Y.; Ge, C.; Ren, M.; Yin, H.; Wang, A.; Zhang, D.; Liu, C.; Chen, J.; Feng, H.; Yao, H.; et al. Effects of coating parameters on the morphology of SiO₂-coated TiO₂ and the pigmentary properties. *Appl. Surf. Sci.* **2008**, *254*, 2809–2819. [[CrossRef](#)]
12. Wu, H.-X.; Wang, T.-J.; Jin, Y. Morphology “phase diagram” of the hydrous alumina coating on TiO₂ particles during aqueous precipitation. *Ind. Eng. Chem. Res.* **2006**, *45*, 5274–5278. [[CrossRef](#)]
13. Simpson, D.J.; Thilagam, A.; Cavallaro, G.P.; Kaplun, K.; Gerson, A.R. SiO₂ coated pure and doped titania pigments: Low temperature CVD deposition and quantum chemical study. *Phys. Chem. Chem. Phys.* **2011**, *13*, 21132–21138. [[CrossRef](#)] [[PubMed](#)]
14. King, D.M.; Liang, X.; Burton, B.B.; Kamal Akhtar, M.; Weimer, A.W. Passivation of pigment-grade TiO₂ particles by nanothick atomic layer deposited SiO₂ films. *Nanotechnology* **2008**, *19*, 255604. [[CrossRef](#)] [[PubMed](#)]
15. Liang, X.; Barrett, K.S.; Jiang, Y.-B.; Weimer, A.W. Rapid silica atomic layer deposition on large quantities of cohesive nanoparticles. *ACS Appl. Mater. Interfaces* **2010**, *2*, 2248–2253. [[CrossRef](#)] [[PubMed](#)]
16. Guo, J.; Yuan, S.; Yu, Y.; van Ommen, J.R.; Van Bui, H.; Liang, B. Room-temperature pulsed CVD-grown SiO₂ protective layer on TiO₂ particles for photocatalytic activity suppression. *RSC Adv.* **2017**, *7*, 4547–4554. [[CrossRef](#)]
17. Seidel, G.R. Production of Improved Titanium Pigments. U.S. Patent 2,387,534, 23 October 1945.
18. Wei, B.-X.; Zhao, L.; Wang, T.-J.; Jin, Y. Detrimental thixotropic thinning of filter cake of SiO₂–Al₂O₃ composite coated TiO₂ particles and its control. *Ind. Eng. Chem. Res.* **2011**, *50*, 13799–13804. [[CrossRef](#)]
19. Wei, B.-X.; Zhao, L.; Wang, T.-J.; Gao, H.; Wu, H.-X.; Jin, Y. Photo-stability of TiO₂ particles coated with several transition metal oxides and its measurement by Rhodamine-B degradation. *Adv. Powder Technol.* **2013**, *24*, 708–713. [[CrossRef](#)]
20. Van Bui, H.; Grillo, F.; van Ommen, J.R. Atomic and molecular layer deposition: Off the beaten track. *Chem. Commun.* **2017**, *53*, 45–71. [[CrossRef](#)] [[PubMed](#)]
21. Puurunen, R.L. Surface chemistry of atomic layer deposition: A case study for the trimethylaluminum/water process. *J. Appl. Phys.* **2005**, *97*, 121301. [[CrossRef](#)]
22. George, S.M. Atomic layer deposition: An overview. *Chem. Rev.* **2010**, *110*, 111–131. [[CrossRef](#)] [[PubMed](#)]
23. Puurunen, R.L. A short history of atomic layer deposition: Tuomo suntola’s atomic layer epitaxy. *Chem. Vap. Depos.* **2014**, *20*, 332–344. [[CrossRef](#)]
24. Malygin, A.A.; Drozd, V.E.; Malkov, A.A.; Smirnov, V.M. From V. B. Aleskovskii’s “framework” hypothesis to the method of molecular layering/atomic layer deposition. *Chem. Vap. Depos.* **2015**, *21*, 216–240. [[CrossRef](#)]
25. Lu, J.; Elam, J.W.; Stair, P.C. Atomic layer deposition—Sequential self-limiting surface reactions for advanced catalyst “bottom-up” synthesis. *Surf. Sci. Rep.* **2016**, *71*, 410–472. [[CrossRef](#)]
26. Johnson, R.W.; Hultqvist, A.; Bent, S.F. A brief review of atomic layer deposition: From fundamentals to applications. *Mater. Today* **2014**, *17*, 236–246. [[CrossRef](#)]
27. Ferguson, J.; Weimer, A.; George, S. Atomic layer deposition of ultrathin and conformal Al₂O₃ films on BN particles. *Thin Solid Films* **2000**, *371*, 95–104. [[CrossRef](#)]

28. Ferguson, J.D.; Weimer, A.W.; George, S.M. Atomic layer deposition of SiO₂ films on BN particles using sequential surface reactions. *Chem. Mater.* **2000**, *12*, 3472–3480. [[CrossRef](#)]
29. Ferguson, J.; Weimer, A.; George, S. Atomic layer deposition of Al₂O₃ films on polyethylene particles. *Chem. Mater.* **2004**, *16*, 5602–5609. [[CrossRef](#)]
30. Ferguson, J.; Smith, E.; Weimer, A.; George, S. ALD of SiO₂ at room temperature using TEOS and H₂O with NH₃ as the catalyst. *J. Electrochem. Soc.* **2004**, *151*, G528–G535. [[CrossRef](#)]
31. Wank, J.R.; George, S.M.; Weimer, A.W. Coating fine nickel particles with Al₂O₃ utilizing an atomic layer deposition-fluidized bed reactor (ALD–FBR). *J. Am. Ceram. Soc.* **2004**, *87*, 762–765. [[CrossRef](#)]
32. McCormick, J.A.; Rice, K.P.; Paul, D.F.; Weimer, A.W.; George, S.M. Analysis of Al₂O₃ atomic layer deposition on ZrO₂ nanoparticles in a rotary reactor. *Chem. Vap. Depos.* **2007**, *13*, 491–498. [[CrossRef](#)]
33. Hakim, L.F.; George, S.M.; Weimer, A.W. Conformal nanocoating of zirconia nanoparticles by atomic layer deposition in a fluidized bed reactor. *Nanotechnology* **2005**, *16*, S375–S381. [[CrossRef](#)] [[PubMed](#)]
34. Valdesueiro, D.; Meesters, G.; Kreutzer, M.; van Ommen, J. Gas-phase deposition of ultrathin aluminium oxide films on nanoparticles at ambient conditions. *Materials* **2015**, *8*, 1249–1263. [[CrossRef](#)] [[PubMed](#)]
35. Duan, C.-L.; Deng, Z.; Cao, K.; Yin, H.-F.; Shan, B.; Chen, R. Surface passivation of Fe₃O₄ nanoparticles with Al₂O₃ via atomic layer deposition in a rotating fluidized bed reactor. *J. Vac. Sci. Technol. A* **2016**, *34*, 04C103. [[CrossRef](#)]
36. Manandhar, K.; Wollmershauser, J.A.; Boercker, J.E.; Feigelson, B.N. Growth per cycle of alumina atomic layer deposition on nano- and micro-powders. *J. Vac. Sci. Technol. A* **2016**, *34*, 021519. [[CrossRef](#)]
37. McCormick, J.A.; Cloutier, B.L.; Weimer, A.W.; George, S.M. Rotary reactor for atomic layer deposition on large quantities of nanoparticles. *J. Vac. Sci. Technol. A* **2007**, *25*, 67–74. [[CrossRef](#)]
38. King, D.M.; Spencer, J.A.; Liang, X.; Hakim, L.F.; Weimer, A.W. Atomic layer deposition on particles using a fluidized bed reactor with in situ mass spectrometry. *Surf. Coat. Technol.* **2007**, *201*, 9163–9171. [[CrossRef](#)]
39. Beetstra, R.; Lafont, U.; Nijenhuis, J.; Kelder, E.M.; van Ommen, J.R. Atmospheric pressure process for coating particles using atomic layer deposition. *Chem. Vap. Depos.* **2009**, *15*, 227–233. [[CrossRef](#)]
40. Hakim, L.F.; King, D.M.; Zhou, Y.; Gump, C.J.; George, S.M.; Weimer, A.W. Nanoparticle coating for advanced optical, mechanical and rheological properties. *Adv. Funct. Mater.* **2007**, *17*, 3175–3181. [[CrossRef](#)]
41. Ritala, M.; Leskelä, M.; Dekker, J.P.; Mutsaers, C.; Soininen, P.J.; Skarp, J. Perfectly conformal tin and Al₂O₃ films deposited by atomic layer deposition. *Chem. Vap. Depos.* **1999**, *5*, 7–9. [[CrossRef](#)]
42. Elam, J.W.; Routkevitch, D.; Mardilovich, P.P.; George, S.M. Conformal coating on ultrahigh-aspect-ratio nanopores of anodic alumina by atomic layer deposition. *Chem. Mater.* **2003**, *15*, 3507–3517. [[CrossRef](#)]
43. Dendooven, J.; Deduytsche, D.; Musschoot, J.; Vanmeirhaeghe, R.L.; Detavernier, C. Conformality of Al₂O₃ and AlN deposited by plasma-enhanced atomic layer deposition. *J. Electrochem. Soc.* **2010**, *157*, G111–G116. [[CrossRef](#)]
44. Berland, B.S.; Gartland, I.P.; Ott, A.W.; George, S.M. In situ monitoring of atomic layer controlled pore reduction in alumina tubular membranes using sequential surface reactions. *Chem. Mater.* **1998**, *10*, 3941–3950. [[CrossRef](#)]
45. Elam, J.W.; Xiong, G.; Han, C.Y.; Wang, H.H.; Birrell, J.P.; Welp, U.; Hryn, J.N.; Pellin, M.J.; Baumann, T.F.; Poco, J.F.; et al. Atomic layer deposition for the conformal coating of nanoporous materials. *J. Nanomater.* **2006**, *2006*, 64501. [[CrossRef](#)]
46. Levrau, E.; Van de Kerckhove, K.; Devloo-Casier, K.; Pulinthanathu Sree, S.; Martens, J.A.; Detavernier, C.; Dendooven, J. In situ IR spectroscopic investigation of alumina ALD on porous silica films: Thermal versus plasma-enhanced ALD. *J. Phys. Chem. C* **2014**, *118*, 29854–29859. [[CrossRef](#)]
47. Valdesueiro, D.; Prabhu, M.K.; Guerra-Nunez, C.; Sandeep, C.S.S.; Kinge, S.; Siebbeles, L.D.A.; de Smet, L.C.P.M.; Meesters, G.M.H.; Kreutzer, M.T.; Houtepen, A.J.; et al. Deposition mechanism of aluminum oxide on quantum dot films at atmospheric pressure and room temperature. *J. Phys. Chem. C* **2016**, *120*, 4266–4275. [[CrossRef](#)]
48. Mirvakili, M.N.; Van Bui, H.; van Ommen, J.R.; Hatzikiriakos, S.G.; Englezos, P. Enhanced barrier performance of engineered paper by atomic layer deposited Al₂O₃ thin films. *ACS Appl. Mater. Interfaces* **2016**, *8*, 13590–13600. [[CrossRef](#)] [[PubMed](#)]
49. Farmer, D.B.; Gordon, R.G. Atomic layer deposition on suspended single-walled carbon nanotubes via gas-phase noncovalent functionalization. *Nano Lett.* **2006**, *6*, 699–703. [[CrossRef](#)] [[PubMed](#)]

50. Cavanagh, A.S.; Wilson, C.A.; Weimer, A.W.; George, S.M. Atomic layer deposition on gram quantities of multi-walled carbon nanotubes. *Nanotechnology* **2009**, *20*, 255602. [[CrossRef](#)] [[PubMed](#)]
51. Lee, B.; Park, S.-Y.; Kim, H.-C.; Cho, K.; Vogel, E.M.; Kim, M.J.; Wallace, R.M.; Kim, J. Conformal Al₂O₃ dielectric layer deposited by atomic layer deposition for graphene-based nanoelectronics. *Appl. Phys. Lett.* **2008**, *92*, 203102. [[CrossRef](#)]
52. Young, M.J.; Musgrave, C.B.; George, S.M. Growth and characterization of Al₂O₃ atomic layer deposition films on sp²-graphitic carbon substrates using NO₂/trimethylaluminum pretreatment. *ACS Appl. Mater. Interfaces* **2015**, *7*, 12030–12037. [[CrossRef](#)] [[PubMed](#)]
53. Zheng, L.; Cheng, X.; Cao, D.; Wang, G.; Wang, Z.; Xu, D.; Xia, C.; Shen, L.; Yu, Y.; Shen, D. Improvement of Al₂O₃ films on graphene grown by atomic layer deposition with pre-H₂O treatment. *ACS Appl. Mater. Interfaces* **2014**, *6*, 7014–7019. [[CrossRef](#)] [[PubMed](#)]
54. Wilson, C.; Grubbs, R.; George, S. Nucleation and growth during Al₂O₃ atomic layer deposition on polymers. *Chem. Mater.* **2005**, *17*, 5625–5634. [[CrossRef](#)]
55. Knez, M.; Kadri, A.; Wege, C.; Gösele, U.; Jeske, H.; Nielsch, K. Atomic layer deposition on biological macromolecules: Metal oxide coating of tobacco mosaic virus and ferritin. *Nano Lett.* **2006**, *6*, 1172–1177. [[CrossRef](#)] [[PubMed](#)]
56. Dillon, A.; Ott, A.; Way, J.; George, S. Surface chemistry of Al₂O₃ deposition using Al(CH₃)₃ and H₂O in a binary reaction sequence. *Surf. Sci.* **1995**, *322*, 230–242. [[CrossRef](#)]
57. Rahtu, A.; Alaranta, T.; Ritala, M. In situ quartz crystal microbalance and quadrupole mass spectrometry studies of atomic layer deposition of aluminum oxide from trimethylaluminum and water. *Langmuir* **2001**, *17*, 6506–6509. [[CrossRef](#)]
58. Widjaja, Y.; Musgrave, C.B. Quantum chemical study of the mechanism of aluminum oxide atomic layer deposition. *Appl. Phys. Lett.* **2002**, *80*, 3304–3306. [[CrossRef](#)]
59. Elliott, S.D.; Greer, J.C. Simulating the atomic layer deposition of alumina from first principles. *J. Mater. Chem.* **2004**, *14*, 3246–3250. [[CrossRef](#)]
60. Puurunen, R.L.; Vandervorst, W.; Besling, W.F.A.; Richard, O.; Bender, H.; Conard, T.; Zhao, C.; Delabie, A.; Caymax, M.; De Gendt, S.; et al. Island growth in the atomic layer deposition of zirconium oxide and aluminum oxide on hydrogen-terminated silicon: Growth mode modeling and transmission electron microscopy. *J. Appl. Phys.* **2004**, *96*, 4878–4889. [[CrossRef](#)]
61. Groner, M.; Fabreguette, F.; Elam, J.; George, S. Low-temperature Al₂O₃ atomic layer deposition. *Chem. Mater.* **2004**, *16*, 639–645. [[CrossRef](#)]
62. Wind, R.A.; George, S.M. Quartz crystal microbalance studies of Al₂O₃ atomic layer deposition using trimethylaluminum and water at 125 °C. *J. Phys. Chem. A* **2009**, *114*, 1281–1289. [[CrossRef](#)] [[PubMed](#)]
63. Potts, S.E.; Keuning, W.; Langereis, E.; Dingemans, G.; van de Sanden, M.C.M.; Kessels, W.M.M. Low temperature plasma-enhanced atomic layer deposition of metal oxide thin films. *J. Electrochem. Soc.* **2010**, *157*, P66–P74. [[CrossRef](#)]
64. Shirazi, M.; Elliott, S.D. Cooperation between adsorbates accounts for the activation of atomic layer deposition reactions. *Nanoscale* **2015**, *7*, 6311–6318. [[CrossRef](#)] [[PubMed](#)]
65. Vandalon, V.; Kessels, W.M.M. What is limiting low-temperature atomic layer deposition of Al₂O₃? A vibrational sum-frequency generation study. *Appl. Phys. Lett.* **2016**, *108*, 011607. [[CrossRef](#)]
66. Guerra-Nuñez, C.; Döbeli, M.; Michler, J.; Utke, I. Reaction and growth mechanisms in Al₂O₃ deposited via atomic layer deposition: Elucidating the hydrogen source. *Chem. Mater.* **2017**, *29*, 8690–8703. [[CrossRef](#)]
67. Lownsbury, J.M.; Gladden, J.A.; Campbell, C.T.; Kim, I.S.; Martinson, A.B.F. Direct measurements of half-cycle reaction heats during atomic layer deposition by calorimetry. *Chem. Mater.* **2017**, *29*, 8566–8577. [[CrossRef](#)]
68. Puurunen, R.L.; Lindblad, M.; Root, A.; Outi, I.; Krause, A. Successive reactions of gaseous trimethylaluminum and ammonia on porous alumina. *Phys. Chem. Chem. Phys.* **2001**, *3*, 1093–1102. [[CrossRef](#)]
69. Ishida, M.; Eto, A.; Nakamura, T.; Suzuki, T. Decomposition of trimethylaluminum and N₂O on Si surfaces using ultraviolet laser photolysis to produce Al₂O₃ films. *J. Vac. Sci. Technol. A* **1989**, *7*, 2931–2934. [[CrossRef](#)]
70. Gow, T.; Lin, R.; Cadwell, L.; Lee, F.; Backman, A.; Masel, R.I. Decomposition of trimethylaluminum on silicon (100). *Chem. Mater.* **1989**, *1*, 406–411. [[CrossRef](#)]
71. Mayer, T.M.; Rogers, J., Jr.; Michalske, T. Mechanism of nucleation and atomic layer growth of aluminum nitride on silicon. *Chem. Mater.* **1991**, *3*, 641–646. [[CrossRef](#)]

72. Van Bui, H.; Wiggers, F.; Friedlein, R.; Yamada-Takamura, Y.; Kovalgin, A.; de Jong, M. On the feasibility of silicene encapsulation by AlN deposited using an atomic layer deposition process. *J. Chem. Phys.* **2015**, *142*, 064702. [[CrossRef](#)] [[PubMed](#)]
73. Juppo, M.; Rahtu, A.; Ritala, M.; Leskelä, M. In situ mass spectrometry study on surface reactions in atomic layer deposition of Al₂O₃ thin films from trimethylaluminum and water. *Langmuir* **2000**, *16*, 4034–4039. [[CrossRef](#)]
74. Ylivaara, O.M.E.; Liu, X.; Kilpi, L.; Lyytinen, J.; Schneider, D.; Laitinen, M.; Julin, J.; Ali, S.; Sintonen, S.; Berdova, M.; et al. Aluminum oxide from trimethylaluminum and water by atomic layer deposition: The temperature dependence of residual stress, elastic modulus, hardness and adhesion. *Thin Solid Films* **2014**, *552*, 124–135. [[CrossRef](#)]
75. Liang, X.; Hakim, L.F.; Zhan, G.-D.; McCormick, J.A.; George, S.M.; Weimer, A.W.; Spencer, J.A.; Buechler, K.J.; Blackson, J.; Wood, C.J.; et al. Novel processing to produce polymer/ceramic nanocomposites by atomic layer deposition. *J. Am. Ceram. Soc.* **2007**, *90*, 57–63. [[CrossRef](#)]
76. Jensen, H.; Soloviev, A.; Li, Z.; Søgaaard, E.G. XPS and FTIR investigation of the surface properties of different prepared titania nano-powders. *Appl. Surf. Sci.* **2005**, *246*, 239–249. [[CrossRef](#)]
77. Benkoula, S.; Sublemontier, O.; Patanen, M.; Nicolas, C.; Sirotti, F.; Naitabdi, A.; Gaie-Levrel, F.; Antonsson, E.; Aureau, D.; Ouf, F.X.; et al. Water adsorption on TiO₂ surfaces probed by soft X-ray spectroscopies: Bulk materials vs. Isolated nanoparticles. *Sci. Rep.* **2015**, *5*, 15088. [[CrossRef](#)] [[PubMed](#)]
78. Jankovský, O.; Šimek, P.; Sedmidubský, D.; Huber, Š.; Pumera, M.; Sofer, Z. Towards highly electrically conductive and thermally insulating graphene nanocomposites: Al₂O₃–graphene. *RSC Adv.* **2014**, *4*, 7418–7424. [[CrossRef](#)]
79. Chen, A.H.; Liang, L.Y.; Zhang, H.Z.; Liu, Z.M.; Ye, X.J.; Yu, Z.; Cao, H.T. Enhancement of a-IZO TTFT performance by using Y₂O₃/Al₂O₃ bilayer dielectrics. *Electrochem. Solid-State Lett.* **2011**, *14*, H88–H92. [[CrossRef](#)]
80. Iatsunskiy, I.; Kempniński, M.; Jancelewicz, M.; Załęski, K.; Jurga, S.; Smyntyna, V. Structural and XPS characterization of ALD Al₂O₃ coated porous silicon. *Vacuum* **2015**, *113*, 52–58. [[CrossRef](#)]
81. Reddy, K.M.; Manorama, S.V.; Reddy, A.R. Bandgap studies on anatase titanium dioxide nanoparticles. *Mater. Chem. Phys.* **2003**, *78*, 239–245. [[CrossRef](#)]
82. Spicer, P.T.; Artelt, C.; Sanders, S.; Pratsinis, S.E. Flame synthesis of composite carbon black-fumed silica nanostructured particles. *J. Aerosol Sci.* **1998**, *29*, 647–659. [[CrossRef](#)]
83. Mueller, R.; Kammler, H.K.; Wegner, K.; Pratsinis, S.E. OH surface density of SiO₂ and TiO₂ by thermogravimetric analysis. *Langmuir* **2003**, *19*, 160–165. [[CrossRef](#)]
84. Moniz, S.J.A.; Tang, J. Charge transfer and photocatalytic activity in CuO/TiO₂ nanoparticle heterojunctions synthesised through a rapid, one-pot, microwave solvothermal route. *ChemCatChem* **2015**, *7*, 1659–1667. [[CrossRef](#)]
85. Jang, E.; Sridharan, K.; Park, Y.M.; Park, T.J. Eliminated phototoxicity of TiO₂ particles by an atomic-layer-deposited Al₂O₃ coating layer for UV-protection applications. *Chem. Eur. J.* **2016**, *22*, 12022–12026. [[CrossRef](#)] [[PubMed](#)]
86. Liang, X.; Weimer, A.W. Photoactivity passivation of TiO₂ nanoparticles using molecular layer deposited (MLD) polymer films. *J. Nanopart. Res.* **2009**, *12*, 135–142. [[CrossRef](#)]
87. Gao, H.; Qiao, B.; Wang, T.-J.; Wang, D.; Jin, Y. Cerium oxide coating of titanium dioxide pigment to decrease its photocatalytic activity. *Ind. Eng. Chem. Res.* **2014**, *53*, 189–197. [[CrossRef](#)]
88. Simonsen, M.E.; Li, Z.; Søgaaard, E.G. Influence of the OH groups on the photocatalytic activity and photoinduced hydrophilicity of microwave assisted sol–gel TiO₂ film. *Appl. Surf. Sci.* **2009**, *255*, 8054–8062. [[CrossRef](#)]
89. Di Paola, A.; Bellardita, M.; Palmisano, L.; Barbieriková, Z.; Brezová, V. Influence of crystallinity and OH surface density on the photocatalytic activity of TiO₂ powders. *J. Photochem. Photobiol. A Chem.* **2014**, *273*, 59–67. [[CrossRef](#)]
90. Sclafani, A.; Palmisano, L.; Schiavello, M. Influence of the preparation methods of titanium dioxide on the photocatalytic degradation of phenol in aqueous dispersion. *J. Phys. Chem.* **1990**, *94*, 829–832. [[CrossRef](#)]

91. Zhang, J.; Zhou, P.; Liu, J.; Yu, J. New understanding of the difference of photocatalytic activity among anatase, rutile and brookite TiO₂. *Phys. Chem. Chem. Phys.* **2014**, *16*, 20382–20386. [[CrossRef](#)] [[PubMed](#)]



© 2018 by the authors. Licensee MDPI, Basel, Switzerland. This article is an open access article distributed under the terms and conditions of the Creative Commons Attribution (CC BY) license (<http://creativecommons.org/licenses/by/4.0/>).